Journal of Applied Geophysics 109 (2014) 71–79

Contents lists available at ScienceDirect

Journal of Applied Geophysics

journal homepage: www.elsevier.com/locate/jappgeo

Gaussian beam based finite-frequency turning wave tomography

Yu Geng *, Xiao-Bi Xie

Institute of Geophysics and Planetary Physics, University of California at Santa Cruz, Santa Cruz, CA 95060, USA

ARTICLE INFO

Article history:
Received 24 May 2014
Accepted 24 July 2014
Available online 1 August 2014

Keywords:
Gaussian beam
Finite-frequency sensitivity kernel
Turning wave
Seismic tomography

ABSTRACT

We introduce a Gaussian beam based method to calculate finite-frequency sensitivity kernels and use these kernels in seismic turning-wave tomography. The Gaussian beam summation method has the advantage of high computation efficiency and without any angle limitation. Thus, it is suitable in generating sensitivity kernels for high-frequency, long-distance and wide-angle waves, particularly for turning waves in models with vertical velocity gradient. We first validate the Gaussian beam calculated sensitivity kernels by comparing them with those calculated using analytical and finite-difference solutions. Then, we build an inversion system based on these kernels for turning wave travel-time tomography. The proposed method incorporates the wave phenomena into the inversion, avoiding drawbacks usually encountered by the high-frequency asymptotic method. On the other hand, this method still keeps the simplicity of the ray-based travel-time tomography. The numerical results are used to demonstrate the potential applications of this method in building velocity models using turning waves.

1. Introduction

Turning wave data are widely used for investigating subsurface velocities both at shallow and great depths. Traditionally, the turning-wave tomography was dominated by the ray-tracing method and based on the first arrival data (Bais et al., 2003; Simmons, 2008; Stefani, 1995; Zhu et al., 1992, 2008). Ray theory is built on the asymptotic approximation and assumes infinitely high frequencies. It often encounters difficulties when handling wave phenomena such as dispersion, scattering and focusing/defocusing. Faced with ever complicated velocity models and today's broadband seismic data, the wave related phenomena in the inversion process cannot be neglected. Thus, wave equation based methods gradually gain their ground and are reported to provide better results in both tomography (Devaney, 1984; Jocker et al., 2006; Luo and Schuster, 1991; Slaney et al., 1984; Spetzler and Snieder, 2004; Woodward, 1992; Wu and Toksoz, 1987; Zhao et al., 2000) and migration velocity analysis (de Hoop et al., 2006; Fliedner and Bevc, 2008; Sava and Biondi, 2004; Xie and Yang, 2008a). Finite-frequency sensitivity kernels, also known as Fréchet kernels (Tarantola, 1987), are introduced in velocity tomography to replace the ray-based method (Dahlen et al., 2000; Huang et al., 2000; Liu et al., 2009; Marquering et al., 1998; Marquering et al., 1999; Tian et al., 2007; Woodward, 1992; Xie and Yang, 2008a). The kernel relates the sensitivity of finite-frequency waves to velocity perturbations in the model. It replaces the ray path and plays the central role mapping the observed travel time residuals to velocity perturbations in tomography inversion.

Several methods have been proposed to calculate finite-frequency sensitivity kernels. The method based on the full-wave finite-difference (FD) calculation (e.g., Zhao et al., 2005) can deal with complex velocity models but is very time consuming. Alternatively, the one-way wave equation based propagator is efficient and can properly handle wave phenomena such as scattering, diffraction and interference. Thus it can be used to calculate finite-frequency kernels (e.g., Fliedner and Bevc, 2008; Xie and Yang, 2008a). However, the angle limitation sometimes prevents it from being used in wide-angle cases. Xie and Pajchel (2014), Xie et al. (2014) used horizontal one-way propagator to calculate sensitivity kernels for wide-angle turning waves and used them in tomography. The Gaussian beam (GB) is an asymptotic solution to the wave equation and constructed in a curvilinear coordinate system (Cerveny, 1985; Popov, 1982). This method has been widely used in seismic modeling and imaging (Gray, 2005; Hill, 1990, 2001; Nowack, 2008; Nowack and Aki, 1984; Popov et al., 2010). At high-frequencies, wavefield can be expressed as the summation of multiple GBs. Compared to the geometrical ray, the GB overcomes some critical difficulties such as the two-point ray tracing and focusing/defocusing issues. Compared to the full-wave equation, the GB method is very efficient, particularly at high frequencies and for long propagation distance. Compared to the one-way propagator, the GB method does not have angle limitation, thus can handle wide-angle waves including turning waves.

In this paper, we demonstrate how to use the GB method to calculate finite-frequency sensitivity kernels, and test its applications in turning wave tomography. We first validate GB based kernels by comparing

* Corresponding author. Tel.: +1 831 332 6247, +1 613 600 7010.
E-mail address: gengfish@gmail.com (Y. Geng).

http://dx.doi.org/10.1016/j.jappgeo.2014.07.019
0926-9851/

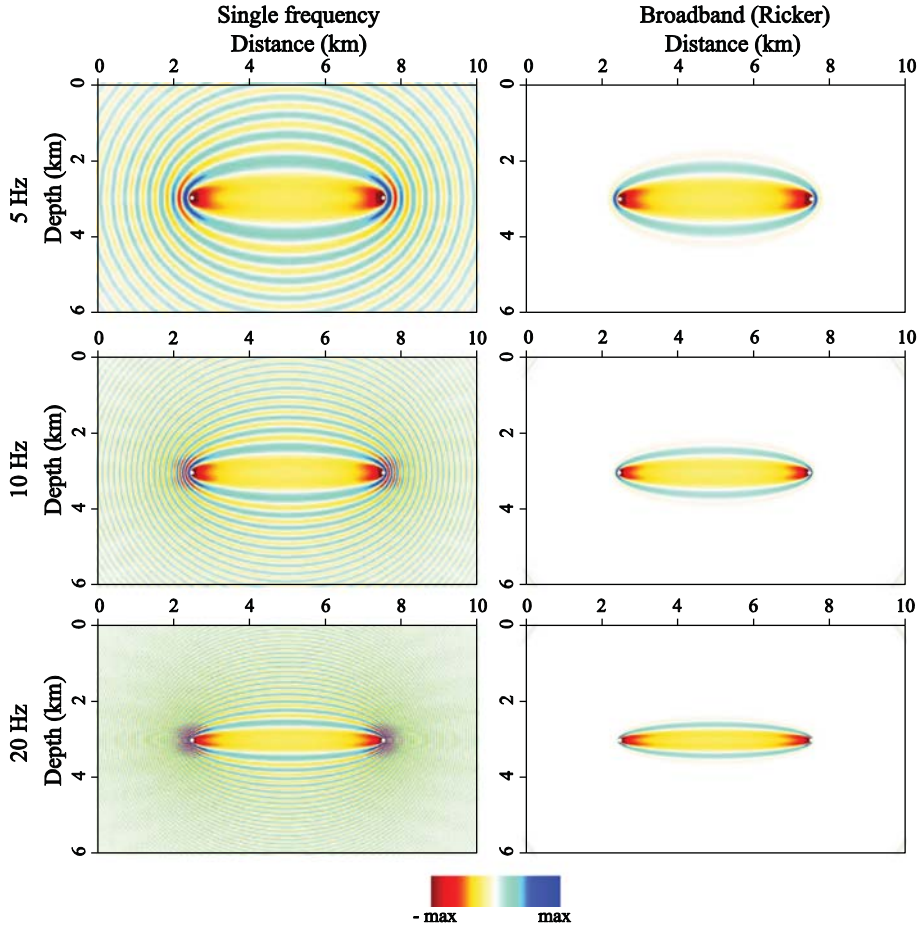

Fig. 1. Monotonic (left column) and broadband (right column) sensitivity kernels calculated using the GB method. Different rows are for different frequencies. The distance between the source and the receiver is 5 km. The colors shown in the figure are normalized sensitivities.

them with more accurate analytical and FD solutions. We also compare kernel predicted travel-time delays with those directly measured from wave propagations. Finally, we create an inversion system based on sensitivity kernels and use synthetic data set to test its applications in turning wave tomography.

2. Calculate sensitivity kernels using Gaussian beams

Based on the scattering theory, the frequency domain sensitivity kernel K_F for phase delay can be expressed as (see, e.g., Jocker et al., 2006; Spetzler and Snieder, 2004; Woodward, 1992)

$$K_F(\mathbf{r},\mathbf{r}_S,\mathbf{r}_G,\omega)=\mathrm{imag}\left[2k_0^2\frac{G(\mathbf{r};\mathbf{r}_S,\omega)G(\mathbf{r};\mathbf{r}_G,\omega)}{G(\mathbf{r}_G;\mathbf{r}_S,\omega)}\right], \tag{1}$$

where $k_0=\omega/v_0(\mathbf{r})$ is the background wavenumber, ω is the frequency, $v_0(\mathbf{r})$ is the background velocity, G is the Green's function in background model, $\mathbf{r}$ is the space location, $\mathbf{r}_S$ and $\mathbf{r}_G$ are the source and receiver locations, and $imag(\cdot)$ denotes taking imaginary part. The broadband sensitivity kernel for travel time can be obtained by stacking single-frequency kernels

$$K_B(\mathbf{r},\mathbf{r}_S,\mathbf{r}_G)=\int\frac{W(\omega)}{\omega}K_F(\mathbf{r},\mathbf{r}_S,\mathbf{r}_G,\omega)d\omega, \tag{2}$$

where

$$W(\omega)=\frac{\omega^2P(\omega)}{\int\omega^2P(\omega)d\omega} \tag{3}$$

is a weighting function, and $P(\omega)=S(\omega)S^*(\omega)$ is the power spectrum of the source spectrum $S(\omega)$ (Xie and Yang, 2008a).

The sensitivity kernel links the observed travel time residual $\delta t(\mathbf{r}_S,\mathbf{r}_G)$ to the unknown velocity perturbation δv through an integral equation

$$\delta t(\mathbf{r}_S,\mathbf{r}_G)=\int\frac{\delta v}{v_0}K_B(\mathbf{r},\mathbf{r}_S,\mathbf{r}_G)dV, \tag{4}$$

where the spatial integral $\int dV$ includes all regions with nonzero velocity perturbations.

From Eqs. (1) and (2), the calculation of sensitivity kernels is mainly calculating Green's functions in the background velocity models. In frequency domain, the Green's function satisfies the wave equation

$$\nabla^2G(\mathbf{r};\mathbf{r}_S,\omega)+\frac{\omega^2}{v^2}G(\mathbf{r};\mathbf{r}_S,\omega)=-4\pi\delta(\mathbf{r}_S), \tag{5}$$

where $\delta(\mathbf{r}_S)$ is a point source. Taking 2D case as an example, the Green's function can be written as the summation of Gaussian

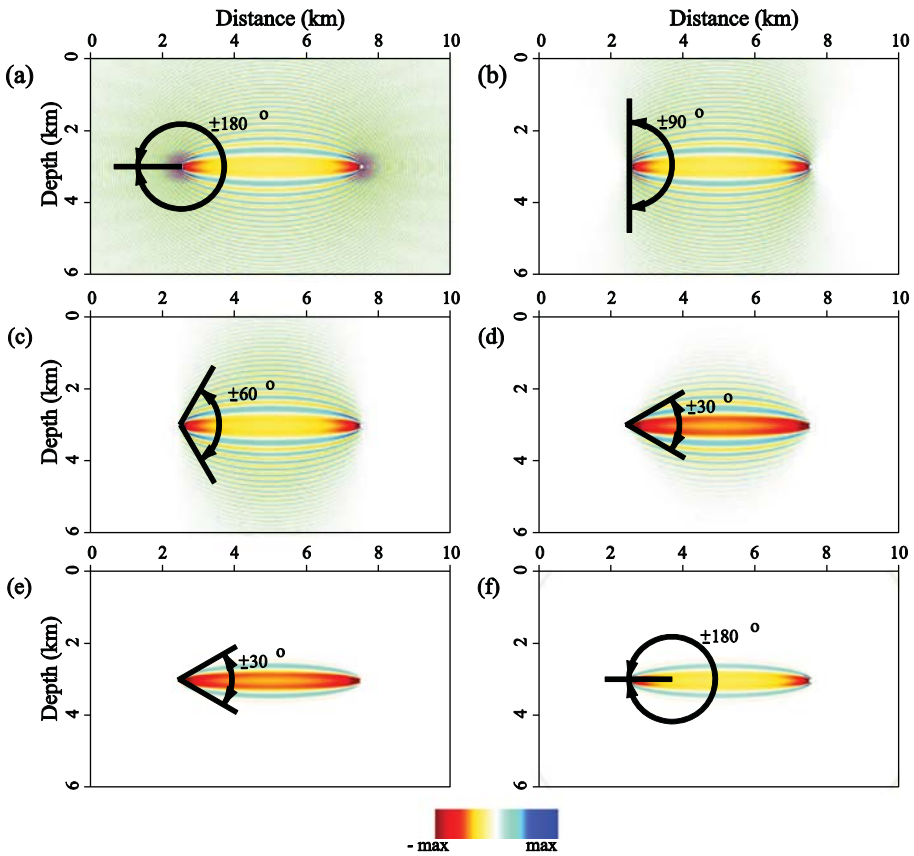

Fig. 2. 20 Hz sensitivity kernels calculated using GB Green's functions with different radiation-angle coverage, where (a) through (d) are monotonic kernels with angle coverage of ±180°, ±90°, ±60°, and ±30°, and (e) and (f) are broadband kernels with angle coverage of ±30° and ±180°. The colors shown in the figure are normalized sensitivities.

beams over ray emergency angle θ (Cerveny, 1982; Hill, 1990; Nowack and Aki, 1984)

$$G(\mathbf{r},\mathbf{r}_S;\omega)\approx\frac{i}{2}\int u_{GB}(\mathbf{r},\mathbf{r}_S,\theta,\omega)d\theta, \tag{6}$$

where $u_{GB}(\mathbf{r},\mathbf{r}_S,\theta,\omega)$ is the wavefield at point $\mathbf{r}$ generated by a Gaussian beam departing from $\mathbf{r}_S$ at angle θ. Gaussian beams propagate along their central rays, so they can be more conveniently expressed in the ray-centered coordinate system (Cerveny, 2001; Hill, 1990)

$$u(s,n,\omega)=\left[\frac{Q(s_0)v(s)}{v(s_0)Q(s)}\right]^{1/2}\exp\left[i\omega\tau(s)+\frac{i\omega}{2}\frac{P(s)}{Q(s)}n^2\right], \tag{7}$$

where s is the arc length along the ray path, s_0 is an arbitrary reference length on the ray, n is the perpendicular distance to the ray, τ is the travel time along the ray, and P and Q are complex scalar functions, which can be obtained by solving dynamic ray tracing equations with given initial values $P(s_0)$ and $Q(s_0)$. We choose $s_0=0$ as the ray starting point. According to Hill (1990), we use initial values $P_0=P(s_0)=i/V_0$ and $Q_0=Q(s_0)=\omega_r w_0^2/V_0$, where ω_r, w_0 and V_0 stand for the reference frequency, the initial beam width and the velocity at the source end of the ray, respectively.

After obtaining $u(s,n,\omega)$ in ray-centered coordinate system, we map them back to spatial domain $u_{GB}(\mathbf{r},\mathbf{r}_S,\theta,\omega)$ using coordinate transform (Cerveny, 2001). We then use Eq. (6) to calculate Green's functions, followed by substituting them into Eqs. (1) and (2) to obtain sensitivity kernels. Shown in Fig. 1 are sensitivity kernels calculated using the GB method. A homogeneous velocity of 3 km/s is used and the source time functions are Ricker wavelets with different central frequencies. Illustrated in the left column are monotonic kernels and in the right column are broadband kernels. Different rows are for different frequencies. We call these sensitivity maps "sensitivity kernels" because they tell how a finite-frequency signal radiated from a source can "sense" velocity variations along its way to the receiver. In 2-dimensional case, the unit for the monotonic kernel is radian/km^2 (per square kilometer per relative velocity perturbation caused phase variation) and the unit for the broadband kernel is sec/km^2 (per square kilometer per relative velocity perturbation caused travel time variation). For 3-dimensional case, the square kilometer should be replaced by cubic kilometer. The colors shown in the figure are normalized sensitivities. The sensitive area is apparently broader than a thin geometrical ray. The sensitivity shows both positive and negative signs indicating that the same perturbation may cause either positive or negative travel time delays (or phase delays) depending on its location. For monotonic kernels, its sensitivity shows oscillations in a broad region. The central non-zero region is the first Fresnel zone. For broadband signals, the oscillating parts in the sensitivity kernels are mostly canceled out due to interference and their non-zero sensitivities shrink to the first Fresnel zone linking the source and the receiver. With the increase of frequency, the broadband sensitivity kernel becomes narrower and its behavior approaches a ray.

Several parameters affect the accuracy of the summation in (6) and the corresponding kernels, e.g., the initial beam width, angle interval and coverage. Because the Gaussian beam is constructed under the paraxial ray approximation, the summation (6) is accurate if the beam is narrow, and the initial beam width determines the behavior of Gaussian beam during propagating, e.g., Gaussian

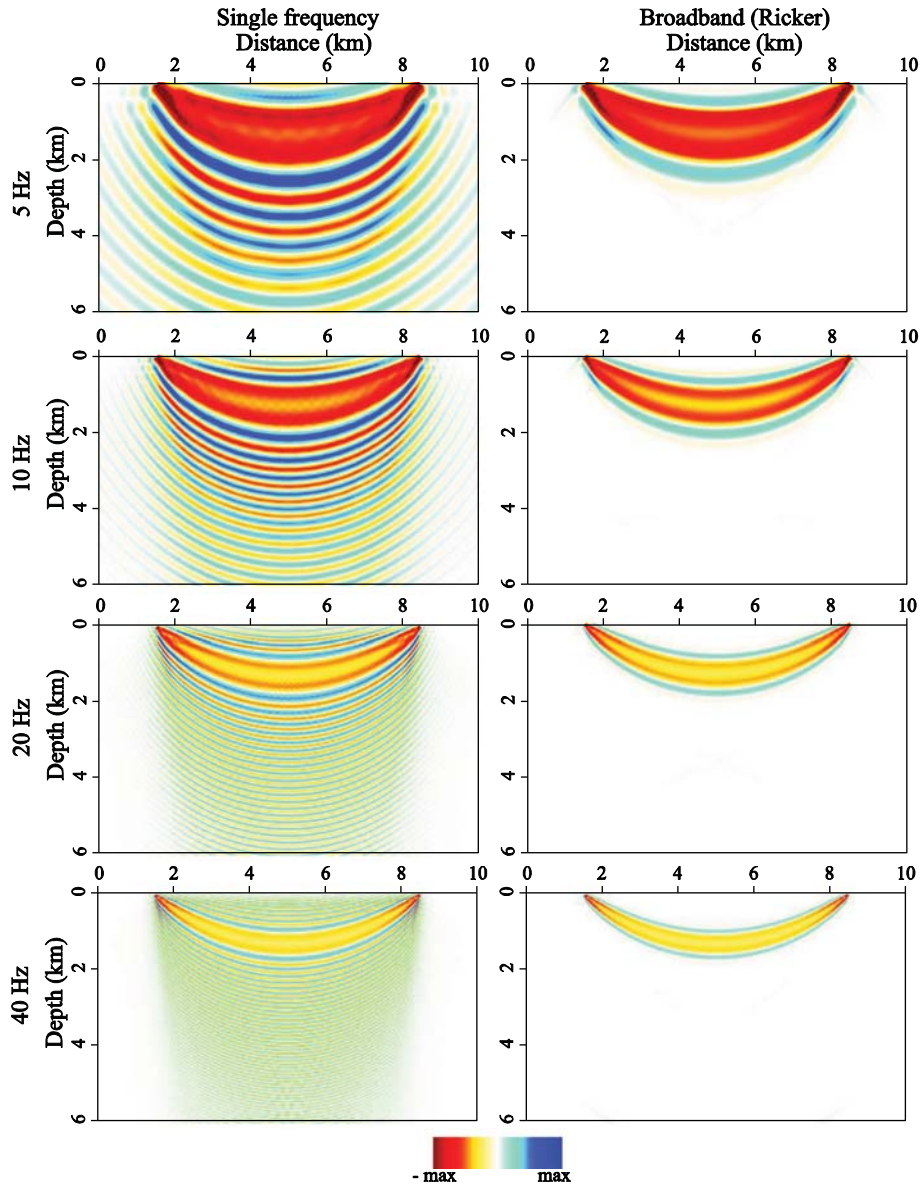

Fig. 3. Sensitivity kernels for turning waves. The colors shown in the figure are normalized sensitivities. Illustrated in the left column are monotonic kernels and in the right column are broadband sensitivity kernels. Individual rows are for different frequencies.

beams with very narrow initial width tend to increase their beam width quickly along with their propagations (Cerveny, 1985; Cerveny et al., 1982; Hill, 1990).Hill (1990) chose to use an initial beam width of

$$w_0 = \frac{2\pi v_a}{\omega_r}, \tag{8}$$

where v_a is half of the average velocity and ω_r is at the lower end of the interested passband. Under this choice, the initial beam width is always larger than the signal wavelength λ. The criterion for choosing angle interval between adjacent GBs in Eq. (6) is

$$\delta\theta \ll \frac{\lambda}{2w_0}. \tag{9}$$

Usually, choosing $\delta\theta \le \lambda/4w_0$ will be good enough for accurate summation. Fig. 2 compares the sensitivity kernels constructed using GB Green's functions with different radiation-angle coverage. Fig. 2a through d are single frequency kernels calculated using radiation angles ranging ±180°, ±90°, ±60°, and ±30°, respectively. The sensitivity kernels calculated using different radiation-angle coverage show differences mostly in the surrounding areas, and particularly around the back-azimuth as related to the receiver direction. These are mostly oscillating areas in a monotonic kernel, while the region in the first Fresnel zone is less affected. For a broadband signal, the sensitive area is mainly in the first Fresnel zone which is described by the broadband kernel. Illustrated in Fig. 2e and f are broadband sensitivity kernels calculated using GB Green's functions with radiation-angle coverage of ±30° and ±180°, respectively. Although the single-frequency kernels show apparent differences, the broadband kernels using different radiation-angle coverage are less affected. Therefore, in a relatively smoothed area, only limited numbers of central rays around the receiver direction are required to compose a high-frequency/long-distance broadband kernel. At other directions, the beams can either be neglected or traced only for a very short distance, which makes this method highly efficient.

The GB method is particularly useful in calculating sensitivity kernels for long distance propagation and at high frequencies. Under this circumstance, other methods are often time-consuming.

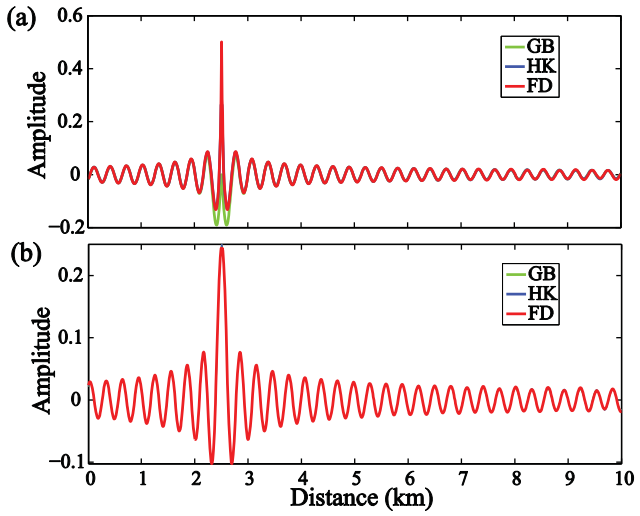

Fig. 4. Comparison of 12 Hz Green's functions calculated using GB, FD and analytical methods, with (a) real part and (b) imaginary part.

In addition, a high-frequency, long-distance kernel usually involves narrower radiation directions. Thus, less central rays are required to compose the Green's functions. The other advantage for the GB method is that it can handle turning waves which are very useful in near-surface seismic tomography and in imaging the steep dip structures in seismic migration. To demonstrate the calculation of turning wave sensitivity kernels, we use a model with 2.0 km/s velocity at the surface, linearly changing to 5.0 km/s at the depth of 6 km.

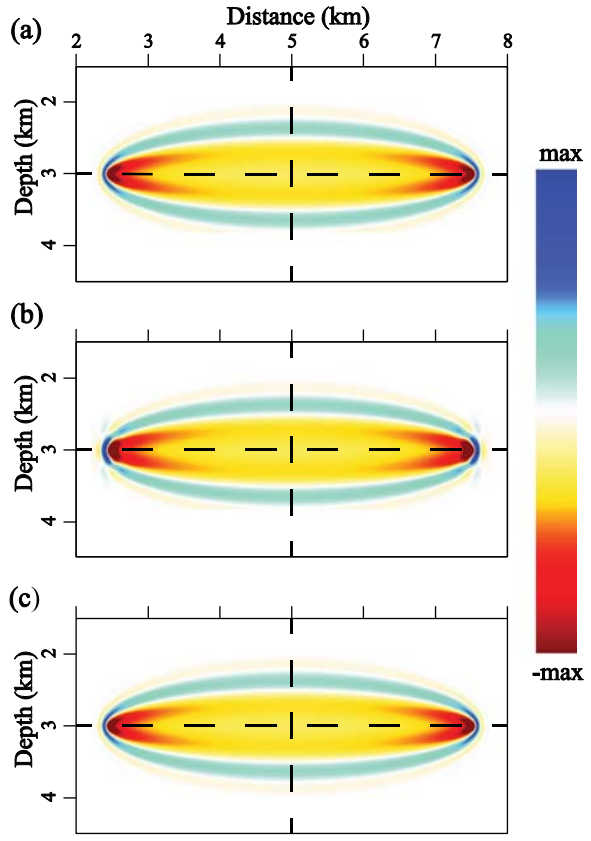

Fig. 5. Sensitivity kernels calculated from (a) FD, (b) GB and (c) analytical solutions. The colors shown in the figure are normalized sensitivities.

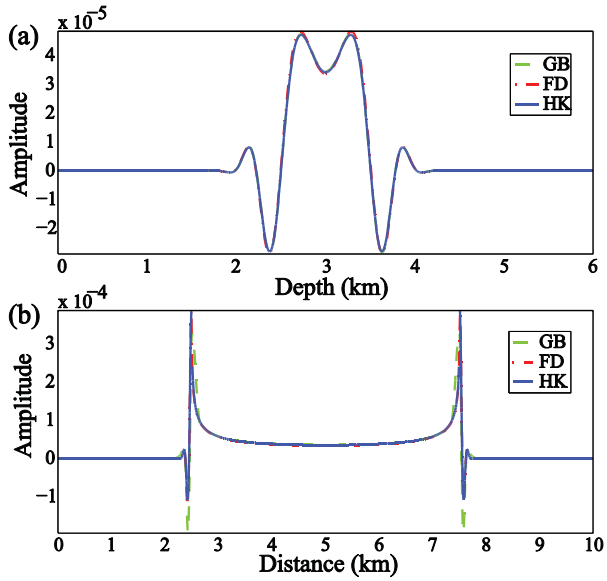

Fig. 6. Selected profiles for kernels in Fig. 2, (a) along the vertical dashed lines, and (b) along the horizontal dashed lines.

Illustrated in Fig. 3 are turning wave sensitivity kernels, where the left and right columns are for monotonic and broadband kernels, and different rows are for different frequencies. We see that turning wave kernel with central frequency up to 40 Hz can be properly handled.

3. Calibration of Gaussian beam based sensitivity kernels

To validate the GB sensitivity kernels, we first compare the analytical, FD and the GB Green's functions in a 2D homogeneous medium with

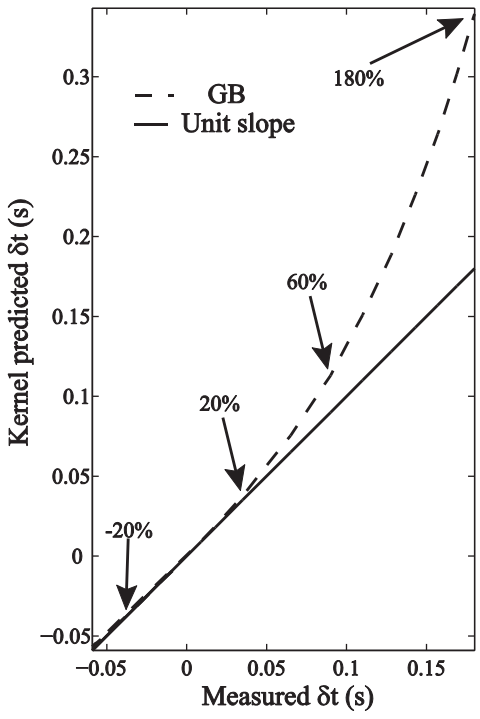

Fig. 7. Comparison between the kernel predicted and directly measured travel time differences. Note the nonlinearity at large perturbations.

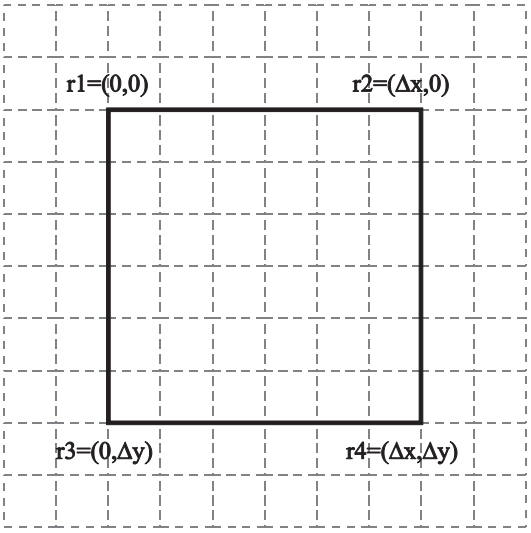

Fig. 8. Coarse grid for model partitioning, where light dashed lines are for original fine velocity grid, and solid lines are for the coarser grid. Δx and Δy are horizontal and vertical sizes of the cell.

$v_0 = 3.5\ km/s$. Under this circumstance, the analytical solution to Eq. (5) is

$$G(\mathbf{r}, \mathbf{r}_S; \omega) = \frac{i}{4} H_0^{(1)}(kr), \tag{10}$$

where $H_0^{(1)}(kr)$ is the zeroth-order first-kind Hankel function, and $r = |\mathbf{r} - \mathbf{r}_s|$. Fig. 4 compares the 12 Hz Green's functions calculated using analytical solution (10), the GB solution (6) and that calculated using a 2D fourth-order acoustic FD algorithm. The results show that, except at the area close to the source, the GB method gives satisfactory accuracy as the analytical and FD solutions. We then compare the broadband sensitivity kernels from a 10 Hz Ricker source to a receiver at a distance of 5 km. The sensitivity kernels calculated using different methods are shown in Fig. 5. Fifty beams are used to form the GB Green's function, and the initial beam width is 0.58 km. The profiles along the two dashed lines in Fig. 5 are shown in Fig. 6. We see different methods give consistent results.

The integral Eq. (4) forms the basis of an inversion system. With sensitivity kernels calculated from the background velocity and travel time data, solving Eq. (4) can obtain velocity perturbation δv. However, Eq. (4) is derived based on the Born approximation, while in reality, the unknown velocity perturbation could be large either in amplitude or in its extension. A velocity perturbation can contribute to the travel time in a nonlinear way, both directly affecting the travel time and indirectly through modifying the shape of the sensitivity kernel. To estimate this nonlinearity, we compare the travel-time differences predicted using Eq. (4) with those directly measured from FD calculations. We use a constant background velocity model with $v_0 = 3.5\ km/s$ and source located at $x = 2.5\ km$ and $z = 3\ km$, and the receiver located at $x = 7.5\ km$ and $z = 3\ km$. A Gaussian shaped circular velocity perturbation patch with a radius of 300 m are centered at $x = 4\ km$ and $z = 3.1\ km$ to generate the travel time differences. The maximum perturbations at the center of the patch are ranging between −30% and 180%. The predicted travel time difference is calculated using Eq. (4) with the sensitivity kernel calculated in the background velocity model. The actual travel-time differences are measured from the cross-correlation between synthetic seismograms calculated by FD method in the background velocity model and the velocity model including the perturbations. Fig. 7 compares the two travel-time differences, where the horizontal and vertical coordinates are for actually measured and the kernel predicted travel time differences. For perturbations between −30% and 60%, their relation is close to the unit slope. However, as expected, under large velocity perturbations, the predicted δt shows apparent deviations from the linear relationship. Under this circumstance, the problem should be linearized and solved in an iterative way.

4. The inversion system

To build a discrete inversion system from (4), we partition the velocity model. Following Xie and Yang (2008b), based on required inversion accuracy, we divide the unknown velocity perturbation $m(\mathbf{r})$ into a coarse grid. Within each rectangular cell, we interpolate the unknown perturbation from the values at four corners $m(\mathbf{r}_1)$, $m(\mathbf{r}_2)$,$m(\mathbf{r}_3)$, $m(\mathbf{r}_4)$ using the hyperbolic function

$$m(\mathbf{r}) = a_1 f_1(\mathbf{r}) + a_2 f_2(\mathbf{r}) + a_3 f_3(\mathbf{r}) + a_4 f_4(\mathbf{r}), \tag{11}$$

where

$$\begin{cases} f_1(\mathbf{r}) = 1 \\ f_2(\mathbf{r}) = x \\ f_3(\mathbf{r}) = y \\ f_4(\mathbf{r}) = xy \end{cases}. \tag{12}$$

Solving Eq. (11) for the four corners, we have the coefficients

$$\begin{pmatrix} a_1 \\ a_2 \\ a_3 \\ a_4 \end{pmatrix} = \begin{pmatrix} 1 & 0 & 0 & 0 \\ -1/\Delta x & 1/\Delta x & 0 & 0 \\ -1/\Delta y & 0 & 1/\Delta y & 0 \\ 1/\Delta x\Delta y & -1/\Delta x\Delta y & -1/\Delta x\Delta y & 1/\Delta x\Delta y \end{pmatrix} \begin{pmatrix} m(\mathbf{r}_1) \\ m(\mathbf{r}_2) \\ m(\mathbf{r}_3) \\ m(\mathbf{r}_4) \end{pmatrix}. \tag{13}$$

where Δx and Δy are horizontal and vertical sizes of the cell (refer to Fig. 8).

Substituting Eq. (11) into Eq. (4) we have

$$\delta t(\mathbf{r}_S, \mathbf{r}_G) = \sum_i \int_{V(\mathbf{r}_i)} m(\mathbf{r}') K_B(\mathbf{r}', \mathbf{r}_S, \mathbf{r}_G) dV' = \sum_i \sum_{j=1}^{4} a_j F K_j, \tag{14}$$

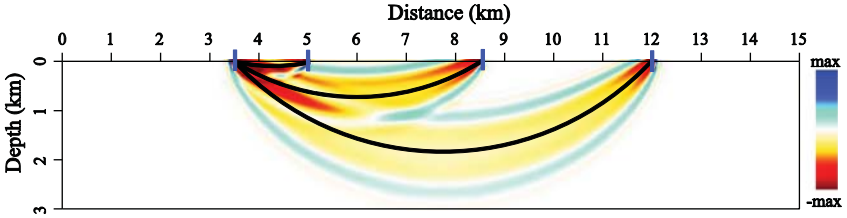

Fig. 9. Sensitivity kernels calculated in the background velocity model, with offsets 1.5 km, 5.0 km and 8.5 km. Solid lines are corresponding central rays. The colors shown in the figure are normalized sensitivities.

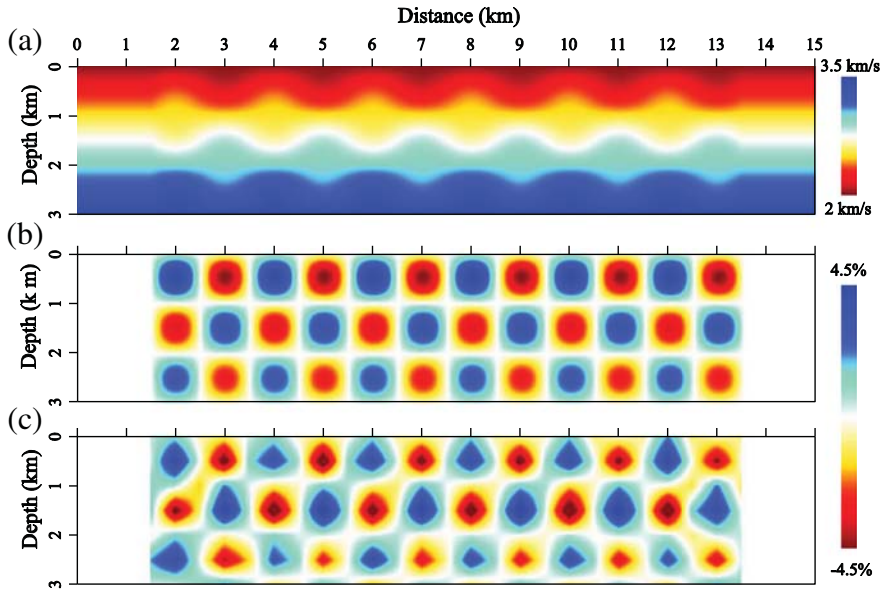

Fig. 10. Resolution test using the checkerboard shaped perturbation, with (a) true velocity model, (b) velocity perturbations and (c) retrieved perturbations.

where

$$FK_j = \int_{V(\mathbf{r}_i)} f_j(\mathbf{r}') K_B(\mathbf{r}', \mathbf{r}_S, \mathbf{r}_G) dV' \tag{15}$$

is the integration within cells $V(\mathbf{r}_i)$. In this way, we do not directly store all sensitivity kernels. Instead, we store only parameters FK_j on four corners of each coarse cell. The Eq. (14) is discretized form of Eq. (4), and will be used in the velocity tomography. The singular value decomposition method (Lawson and Hanson, 1974) will be used to solve Eq. (14) in a least square way.

5. Numerical examples

We use a set of numerical examples to demonstrate the sensitivity kernel based turning wave tomography.

5.1. Resolution test using a checkerboard model

We first test the inversion resolution under the turning wave geometry. As examples, shown in Fig. 9 are 10 Hz broadband turning-wave sensitivity kernels calculated in the background model, of which velocities changing linearly from 2 km/s at the surface to 3.5 km/s at 3 km depth. The true velocity model (Fig. 10a) has a checkerboard shaped perturbation overlapped on the background. The checkerboard has a grid size of 1 km × 1 km and the perturbations vary between ±5%(Fig. 10b). We use a 10 Hz Ricker wavelet as the source time function. To generate large offset data for inversion, we extend the velocity model on both sides, and use 51 shots, each with 28 right sided receivers, to illuminate the model. Both shot and receiver intervals are 0.5 km and the maximum offset is 14 km. The background model also serves as the initial model. The travel-time differences are calculated from synthetic data sets generated using the true velocity

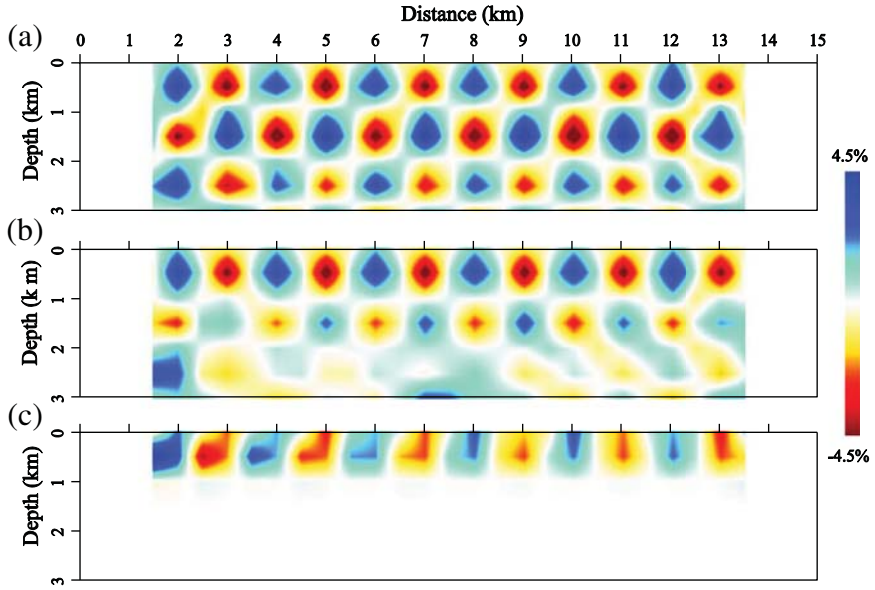

Fig. 11. Inverted checkerboard shaped perturbations using data with different maximum offsets: (a) 12.5 km, (b) 10.5 km and (c) 3 km.

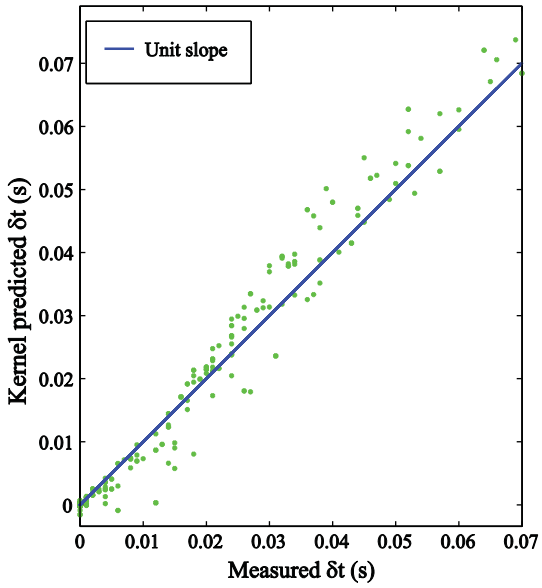

Fig. 12. Comparison between the kernel predicted travel time differences (vertical coordinate) and the δt from synthetic data set (horizontal coordinate). The solid line indicates the unit slope.

model and the background velocity. Shown in Fig. 10c are inverted velocity perturbations. Comparing Fig. 10c with b, the turning wave tomography provides reasonable resolution for the subsurface structures.

In Fig. 9, sensitivity kernels with different offsets penetrate into different depths, thus affecting the resolving depth in inversion. With a similar acquisition system as that used in Fig. 10a, but limit the maximum offsets as 12.5 km, 10.5 km and 3 km in the data, the inversion results are shown in Fig. 11a, b and c, respectively. With the 12.5 km offset, the perturbations down to 3 km depth can be well resolved, while with 3 km offset, only the top 1 km can be inverted. Therefore, in turning wave tomography, long-offset data are important to constrain deeper perturbations.

5.2. Turning wave tomography in a model with high-velocity inclusions

In this example, the true velocity model is composed of a background velocity and a high-velocity patch, shown in Fig. 13a. The background velocity is similar to that used in the previous example and the patch has a maximum perturbation of 8% (shown in Fig. 13b). A 10 Hz Ricker wavelet is used to generate the synthetic data set. A total of 15 shots and 28 fixed receivers are located on the surface between distance 0.5 km and 14.5 km, with shot and receiver intervals are 1 km and 0.5 km, respectively. The background model also serves as the initial model. In Fig. 12, we check the travel time data δt and travel time differences predicted by sensitivity kernels and velocity perturbations. The consistency between two sets of δt values forms the basis of velocity inversion. Shown in Fig. 13c is the inversion result. Comparing Fig. 13c with b, the inverted velocity perturbation reproduces the perturbation pattern with reasonable accuracy. Considering the small perturbations in the model, iterations are not used in the inversion. In Fig. 13c, certain artifacts can still be seen. These are footprints related to the acquisition geometry and model partitioning. They can be removed by increasing data coverage, including smoothing constraint in inversion, or conducting multiple iterations.

6. Conclusion

We proposed using Gaussian beam summation method to calculate finite-frequency sensitivity kernels. The GB method has the advantage of high computation efficiency and no angle limitation, thus suitable for generating sensitivity kernels for wide-angle turning-waves. By comparing these GB generated sensitivity kernels with those calculated using more accurate methods, we validated their accuracy. Additionally, we formulated a turning-wave tomography method based on these sensitivity kernels. The velocity tomography approach based on sensitivity kernels incorporated the wave phenomena into the inversion yet still kept the simplicity of the ray-based tomography. With synthetic data set, we investigated the resolution of the proposed inversion system and demonstrated the successful inversion of the velocity model. It is expected that the proposed method will be useful in building velocity models, particularly in near-surface velocity estimation

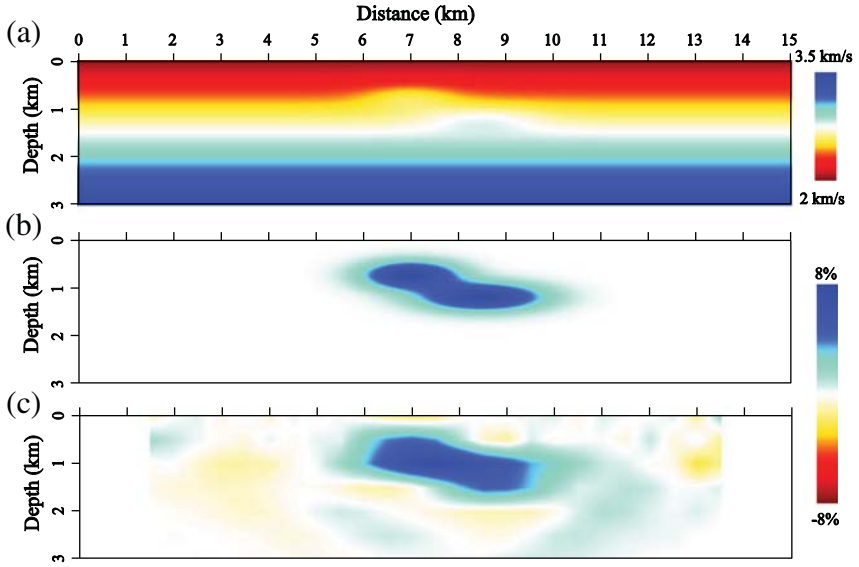

Fig. 13. Turning wave tomography result for a model with a high-velocity inclusion: (a) true velocity model, (b) velocity perturbations and (c) inverted perturbations.

or providing an initial velocity model for more accurate full-waveform inversion.

Acknowledgments

This research is supported by the WTOPI Research Consortium at the University of California, Santa Cruz. We also thank CWP for ray tracing algorithm in SU.

References

Bais, G., Bruno, P.P.G., Di Fiore, V., Rapolla, A., 2003. Characterization of shallow volcanoclastic deposits by turning ray seismic tomography: an application to the Naples urban area. J. Appl. Geophys. 52, 11–21.
Cerveny, V., 1982. Expansion of a plane wave into Gaussian Beams. Stud. Geophys. Geod. 26, 120–131.
Cerveny, V., 1985. Gaussian beam synthetic seismograms. J. Geophys. -Z. Geophys. 58, 44–72.
Cerveny, V., 2001. Seismic Ray Tracing. Cambridge University Press.
Cerveny, V., Popov, M.M., Psencik, I., 1982. Computation of wave fields in inhomogeneous media Gaussian beam approach. Geophys. J. R. Astron. Soc. 70, 109–128.
Dahlen, F.A., Hung, S.H., Nolet, G., 2000. Fréchet kernels for finite-frequency traveltimes—I. Theory. Geophys. J. Int. 141, 157–174.
de Hoop, M.V., van der Hilst, R.D., Shen, P., 2006. Wave-equation reflection tomography: annihilators and sensitivity kernels. Geophys. J. Int. 167, 1332–1352.
Devaney, A.J., 1984. Geophysical diffraction tomography. IEEE Trans. Geosci. Remote Sens. GE-22, 3–13.
Fliedner, M.M., Bevc, D., 2008. Automated velocity model building with wavepath tomography. Geophysics 73, 195–204.
Gray, S.H., 2005. Gaussian beam migration of common-shot records. Geophysics 70, S71–S77.
Hill, N.R., 1990. Gaussian beam migration. Geophysics 55, 1416–1428.
Hill, N.R., 2001. Prestack Gaussian beam depth migration. Geophysics 66, 1240–1250.
Huang, S.H., Dahlen, F.A., Nolet, G., 2000. Fréchet kernels for finite-frequency traveltimes—II. Examples. Geophys. J. Int. 141, 175–203.
Jocker, J., Spetzler, J., Smeulders, D., Trampert, J., 2006. Validation of first-order diffraction theory for the traveltimes and amplitudes of propagating waves. Geophysics 71, T167–T177.
Lawson, C.L., Hanson, R.J., 1974. Solving Least Squares Problems. Prentice-Hall, Inc.
Liu, Y.Z., Dong, L.G., Wang, Y.W., Zhu, J.P., Ma, Z.T., 2009. Sensitivity kernels for seismic Fresnel volume tomography. Geophysics 74, U35–U46.
Luo, Y., Schuster, G.T., 1991. Wave-equation traveltime inversion. Geophysics 56, 645–653.
Marquering, H., Nolet, G., Dahlen, F.A., 1998. Three-dimensional waveform sensitivity kernels. Geophys. J. Int. 132, 521–534.
Marquering, H., Dahlen, F.A., Nolet, G., 1999. Three-dimensional sensitivity kernels for finite-frequency traveltimes: the banana–doughnut paradox. Geophys. J. Int. 137, 805–815.
Nowack, R.L., 2008. Focused Gaussian beams for seismic imaging. . Expanded abstracts SEG 78th AnnualMeet-ing, pp. 2376–2380.
Nowack, R., Aki, K., 1984. The two-dimensional Gaussian beam synthetic method—testing and application. J. Geophys. Res. 89, 7797–7819.
Popov, M.M., 1982. A new method of computation of wave fields using Gaussian beams. Wave Motion 4, 85–97.
Popov, M.M., Semtchenok, N.M., Popov, P.M., Verdel, A.R., 2010. Depth migration by the Gaussian beam summation method. Geophysics 75, S81–S93.
Sava, P., Biondi, B., 2004. Wave-equation migration velocity analysis. I. theory. Geophys. Prospect. 52, 593–606.
Simmons, J.L., 2008. Turning-ray tomography using a low-spatial-frequency model parameterization. Geophysics 73, 93–100.
Slaney, M., Kak, A.C., Larsen, L., 1984. Limitations of imaging with first-order diffraction tomography. IEEE Trans. Microwave Theory Tech. MTT-32, 860–873.
Spetzler, J., Snieder, R., 2004. The Fresnel volume and transmitted waves. Geophysics 69, 653–663.
Stefani, J.P., 1995. Turning-ray tomography. Geophysics 60, 1917–1929.
Tarantola, A., 1987. Inverse Problem Theory. Elsevier Science Publ. Co., Inc.
Tian, Y., Montelli, R., Nolet, G., Dahlen, F.A., 2007. Computing traveltime and amplitude sensitivity kernels in finite-frequency tomography. J. Comput. Phys. 226, 2271–2288.
Woodward, M.J., 1992. Wave-equation tomography. Geophysics 57, 15–26.
Wu, R.S., Toksoz, M.N., 1987. Diffraction tomography and multisource holography applied to seismic imaging. Geophysics 52, 11–25.
Xie, X.B., Pajchel, J., 2014. Velocity tomography based on turning waves and finite-frequency sensitivity kernels. CPS/SEG Beijing 2014 International Geophysical Conference.
Xie, X.B., Yang, H., 2008a. The finite-frequency sensitivity kernel for migration residual moveout and its applications in migration velocity analysis. Geophysics 73, S241–S249.
Xie, X.B., Yang, H., 2008b. A wave-equation migration velocity analysis approach based on the finite-frequency sensitivity kernel. . Expanded abstracts SEG 78th Annual Meeting. 27, pp. 3093–3097.
Xie, X.B., Lokshtanov, D., Pajchel, J., 2014. Finite−frequency sensitivity kernels and turning−wave tomography, possibilities and difficulties, Expanded abstracts SEG 84th Annual Meeting. pp. 4821–4826.
Zhao, L., Jordan, T.H., Chapman, C.H., 2000. Three-dimensional Fréchet differential kernels for seismic delay times. Geophys. J. Int. 141, 558–576.
Zhao, L., Jordan, T.H., Olsen, K.B., Chen, P., 2005. Fréchet kernels for imaging regional earth structure based on three-dimensional reference models. Bull. Seismol. Soc. Am. 95, 2066–2080. http://dx.doi.org/10.1785/0120050081.
Zhu, X.H., Sixta, D.P., Angstman, B.G., 1992. Tomostatics; turning-ray tomography + static corrections. Lead. Edge 11, 15–23.
Zhu, X.H., Valasek, P., Roy, B., Shaw, S., Howell, J., Whitney, S., Whitmore, N.D., Anno, P., 2008. Recent applications of turning-ray tomography. Geophysics 73, 243–254.